A New Inversion Method Based on Distorted Born Iterative Method for Grounded Electrical Source Airborne Transient Electromagnetics

Bingyang Liang, Chen Qiu, Feng Han, Chunhui Zhu, Na Liu, Hai Liu, *Member, IEEE*, Fubo Liu, Guangyou Fang, and Qing Huo Liu, *Fellow, IEEE*

***Abstract*— A new iterative inversion algorithm is proposed to reconstruct the electrical conductivity profile in a stratified underground medium for the grounded electrical source airborne transient electromagnetic (GREATEM) system. In forward modeling, we simplify the mathematical expressions of the magnetic fields generated by a finite line source in the layered ground to semianalytical forms in order to save the computation time. The Fréchet derivative is derived for the electromagnetic response at the receivers due to a small perturbation of the conductivity in a certain layer underground. The initial expression of the Fréchet derivative has an expensive triple integral and contains the Bessel function in the integrand. It is simplified by partially eliminating the integration along the source line and deriving the analytical expression for the integration in the vertical direction inside the perturbed layer. In the inverse solution, we use the distorted Born iterative method (DBIM). This is the first time that the DBIM is applied to data measured by the GREATEM system. Besides, the forward and inverse procedures are carried out in the frequency domain and based on the Fréchet derivative of a line source. We demonstrate the validity of our forward model, Fréchet derivative, inverse model, and the precision as well as robustness of the inversion algorithm through numerical computation and comparisons. Finally, we apply the inversion algorithm to the measured data and compare the retrieved conductivity to the actual drilling data.**

***Index Terms*— 1-D layered media, distorted Born iterative method (DBIM), Fréchet derivative, grounded electrical source airborne transient electromagnetic (GREATEM) survey, semianalytical solution of line source.**

I. Introduction

FOR more than half a century, airborne electromagnetic (AEM) methods have been widely used for large-area resistivity mapping. It is an efficient tool for measuring the subsurface anomalous body under inaccessible areas. The AEM system was first introduced in Canada in 1948 and later successfully carried out in the flight test [1]. Both the AEM system design and algorithm development made great progress in the following decades [2]–[4]. Because of the high resolution of towed bird systems, the AEM has been increasingly used for shallow earth geophysical mapping, such as mineral exploration for iron and molybdenum, ground water surveys, and so on [5]–[9].

However, AEM has some shortcomings, including low accuracy and limited penetration depth, because both the transmitter and the receiver are placed on board an airplane [10], [11]. A semiairborne system called the grounded electrical source airborne transient electromagnetic (GREATEM) system was proposed by Mogi *et al.* [12] to obtain a higher penetration depth. It is also considered to be an airborne version of the long-offset transient electro magnetics system [10]. The GREATEM system uses a grounded electrical line source of 2–3-km long as a transmitter and a three-component magnetometer in the towed bird as the detector [13]. The ground horizontal line source excites electromagnetic (EM) waves with large power that can penetrate deeper into the underground space than the waves generated by dipoles used in the AEM [14], [15]. Other advantages of GREATEM include smaller interferences and the possibility of higher altitude measurements [10].

The data of GREATEM are recorded in the time domain, providing a raw time series of magnetic field excited by the line source on the ground surface and reflected by the underground anomaly. Since the GREATEM is one kind of AEM, the data interpretation methods for them are similar. In the past few years, the AEM data interpretation method had great development with the aid of computer technology. Due to the limitation of the computer ability in the early stage, the image algorithm is the major EM data interpretation method. The image method converts the survey data into some intermediate parameters, such as differential resistivity and conductivity-depth profiles, which reflect the conductivity under ground [16]–[18]. The differential resistivity method [19], conductivity-depth imaging [20], and EM flow method [21] are the most commonly used imaging methods to obtain the characteristics of underground structures. These imaging results can also provide the initial model for inversion. Later, with the development of computer technology, 1-D inversion algorithms appeared, where the underground

Manuscript received March 25, 2017; revised June 3, 2017 and August 18, 2017; accepted September 20, 2017. Date of publication October 9, 2017; date of current version January 26, 2018. This work was supported in part by the National Natural Science Foundation of China under Grant 41390453, Grant 11501481, and Grant 41504120, in part by the Fundamental Research Funds for the Central Universities under Grant 20720160081, and in part by the National Research and Development Projects for Key Scientific Instruments under Grant ZDYZ2012-1-03. *(Corresponding authors: Feng Han; Qing Huo Liu.)*

B. Liang, C. Qiu, F. Han, C. Zhu, N. Liu, and H. Liu are with the Department of Electronic Science, Institute of Electromagnetics and Acoustics, Xiamen University, Xiamen 361005, China (e-mail: feng.han@xmu.edu.cn).

F. Liu and G. Fang are with the Key Laboratory of Electromagnetic Radiation and Sensing Technology, Institute of Electronics, Chinese Academy of Sciences, Beijing 100190, China.

Q. H. Liu is with the Department of Electrical and Computer Engineering, Duke University, Durham, NC 27708 USA (e-mail: qhliu@duke.edu).

Color versions of one or more of the figures in this paper are available online at http://ieeexplore.ieee.org.

Digital Object Identifier 10.1109/TGRS.2017.2756086

0196-2892 © 2017 IEEE. Personal use is permitted, but republication/redistribution requires IEEE permission.
See http://www.ieee.org/publications_standards/publications/rights/index.html for more information.

structure is generally assumed to be a homogeneous or horizontally stratified medium, and thus has no dramatic change in the horizontal direction. So the parameter variation in the vertical direction can be considered as a 1-D profile. The least square method [22] and Occam's inversions [23] are commonly used for 1-D inversion of the AEM data. Usually, in the inversion, the EM response is a nonlinear function of the model parameters. Chen and Raiche [22] and Raiche [24] used the singular value decomposition (SVD) method to solve the 1-D time-domain and frequency-domain inversion problems. Huang and Fraser [19] developed a nonlinear inversion scheme to invert the resistivity. Guillemoteau *et al.* [25] compared different kinds of regularization to obtain a fast and realistic program for time-domain AEM data inversion. These techniques based on least-squares are all downhill searching (gradient) methods, which means that the search of a solution stops when the fitting error is at the bottom of a valley. Occam's inversion is a smooth method that depends weakly on the initial guess [8]. Sattel [26], and Vallée and Smith [27] applied Occam's method to airborne time-domain EM data inversion and obtained stable results. Because there is no lateral correction for Occam's method, the inversions can vary suddenly between stations. A lot of methods have been developed to overcome this disadvantage such as 1-D laterally constrained inversion [28] and holistic inversion [29]. The fundamental approach of all these above-mentioned methods is gradient inversion, which generally starts from an initial model and updates the model iteratively until the difference between the theoretical responses from the updated model and the survey data becomes less than a predetermined threshold. In addition, most of these methods are used to process the EM field data recorded in the time domain and generated by dipole sources in AEM systems.

As the GREATEM system uses a line source, we will establish a new parameterized inversion algorithm to reconstruct the conductivity in the stratified underground medium from magnetic fields excited by the line source in the GREATEM system. The algorithm is carried out in the frequency domain. First, we derive the mathematical expressions in both the forward modeling and Fréchet derivatives and further simplify them by partially eliminating the integration to help save the computation time. We then present the procedure for the inversion algorithm. In the next step, we verify the forward modeling, Fréchet derivatives, as well as the inversion model through a series of numerical experiments, and compare our method with Occam's method. Finally, we apply our algorithm to the measured data and compare the results with the actual drilling data.

II. GREATEM Forward Modeling

In forward modeling, the parameters of the layered ground are known. In order to compute the EM fields excited by a finite-length wire in a GREATEM system, we need to treat the wire as the superposition of many electric dipoles and take the summation of the EM fields excited by all the dipoles [30]. We assume that the ground surface is located at $z = 0$, as shown in Fig. 1. The layer interface is perpendicular to the z-direction and extends to infinity in the xy plane. Layers are indexed from 1 to N in the z-direction, where N is an arbitrary positive integer. The nth layer, with interfaces at $z = z_{n-1}$ and $z = z_n$, is a homogeneous medium with permittivity ϵ_n, permeability μ_n, and conductivity $\sigma_n (n = 1, \ldots, N)$.

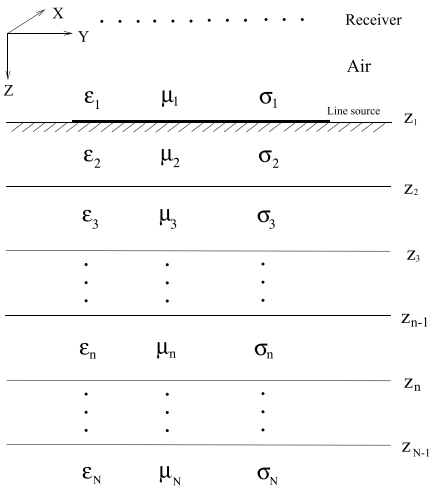

Fig. 1. One-dimensional layered medium model for GREATEM. The finite-length wire source is located on the ground surface.

Maxwell's equations with an electric current source can be expressed as

$$\nabla \times \mathbf{E} = -j\omega\mu\mathbf{H} \tag{1}$$

$$\nabla \times \mathbf{H} = j\omega\tilde{\varepsilon}\mathbf{E} + \mathbf{J} \tag{2}$$

where the complex permittivity is

$$\tilde{\varepsilon} = \varepsilon_0\varepsilon_r + \frac{\sigma}{j\omega}. \tag{3}$$

The current density of a point source in (2) is given as

$$\mathbf{J}(\mathbf{r}) = \mathbf{I}l\delta(\mathbf{r} - \mathbf{r}') \tag{4}$$

where $\mathbf{I}l$ is the electric dipole moment. Using the nomenclature of Michalski and Mosig [31], we can express the EM fields in the spectral k_ρ domain for a dipole current source embedded in a 1-D layered medium as

$$\tilde{\mathbf{E}} = \left\langle \tilde{\mathbf{G}}^{\mathrm{EJ}}; \tilde{\mathbf{J}} \right\rangle \tag{5}$$

$$\tilde{\mathbf{H}} = \left\langle \tilde{\mathbf{G}}^{\mathrm{HJ}}; \tilde{\mathbf{J}} \right\rangle \tag{6}$$

where $\langle , \rangle$ denotes the integral of the product of two functions separated by the comma over their common spectrum support, with a dot over the comma indicating a dot product. $\tilde{\mathbf{G}}^{\mathrm{EJ}}$ and $\tilde{\mathbf{G}}^{\mathrm{HJ}}$ are spectral dyadic Green's functions of the layered medium. $\tilde{\mathbf{J}}$ denotes the dipole source in the spectral domain. $\tilde{\mathbf{E}}$ and $\tilde{\mathbf{H}}$ are the electric and magnetic fields in the spectral domain. By applying the 2-D inverse Fourier transform to (5) and (6), we can obtain the magnetic field in the frequency domain [31]. If the electric dipole source is polarized in the y-direction, the three components of the magnetic field are in the forms of Sommerfeld integrals as

$$\begin{aligned} H_x^d = {} & \frac{1}{2\pi}\int_0^{+\infty} J_0(k_\rho\rho)\frac{(y-y')^2}{{k_\rho}^2}\left(I_i^e + I_i^h\right)k_\rho dk_\rho \\ & - \frac{1}{2\pi}\int_0^{+\infty} J_1(k_\rho\rho)\frac{2(y-y')^2}{{k_\rho}^2}\left(I_i^e - I_i^h\right)k_\rho dk_\rho \\ & + \frac{1}{2\pi}\int_0^{+\infty} J_1(k_\rho\rho)\left(I_i^e - I_i^h\right)\frac{1}{k_\rho\rho}k_\rho dk_\rho \end{aligned} \tag{7}$$

$$H_y^d = -\frac{(y-y')^2}{4\pi k_\rho{}^2}\int_0^{+\infty}\left[J_0(k_\rho\rho)+\frac{2}{k_\rho\rho}J_1(k_\rho\rho)\right]\times\left(I_i^e-I_i^h\right)k_\rho dk_\rho \quad (8)$$

$$H_z^d = -\frac{j(x-x')}{2\pi\omega k_\rho\mu(z)}\int_0^{+\infty}V_i^h J_1(k_\rho\rho)k_\rho dk_\rho \quad (9)$$

where the superscript d means that the field is produced by a dipole source, the coordinate (x', y', z') represents the dipole source location, (x, y, z) denotes the receiver location, ρ is the horizontal distance between the source and the receiver, i.e., $\rho = ((x-x')^2+(y-y')^2)^{1/2}$, k_x, k_y, and k_ρ are the wavenumbers in the x-, y-, and ρ-directions, respectively, I_i^p and V_i^p (the superscript p can be e or h, which represent TM or TE fields) are the current and voltage, respectively, at z due to a 1-A shunt current source at z', which is denoted by the subscript i, J_0 and J_1 are the Bessel functions of the zeroth order and the first order, and $\mu(z)$ is the permeability of the layer in which the receiver is located [31].

Since the magnetic field in (7)–(9) is excited by an infinitesimal electric dipole, the magnetic field generated by a line source along the y-direction for $y\in[-l,l]$ can be obtained by taking the integrals of the three magnetic field components in (7)–(9) with respect to the variable y'. The coordinates of two ends of the line source are $(x', -l, 0)$ and $(x', l, 0)$. Using the method of Rita and Michael [32], we can obtain the magnetic field excited by the line source (denoted by the superscript l) as

$$H_x^l = \frac{1}{2\pi}\frac{y-l}{\rho_+}\int_0^\infty\left(I_i^e-I_i^h\right)J_1(k_\rho\rho_+)dk_\rho - \frac{1}{2\pi}\frac{y+l}{\rho_-}\int_0^\infty\left(I_i^e-I_i^h\right)J_1(k_\rho\rho_-)dk_\rho + \frac{1}{2\pi}\int_{-l}^{l}\int_0^\infty k_\rho I_i^h J_0(k_\rho\rho)dk_\rho dy' \quad (10)$$

$$H_y^l = -\frac{1}{2\pi}\frac{x-x'}{\rho_+}\int_0^\infty\left(I_i^e-I_i^h\right)J_1(k_\rho\rho_+)dk_\rho + \frac{1}{2\pi}\frac{x-x'}{\rho_-}\int_0^\infty\left(I_i^e-I_i^h\right)J_1(k_\rho\rho_-)dk_\rho \quad (11)$$

$$H_z^l = \frac{1}{2\pi}\frac{j}{\omega\tilde{\varepsilon}_v(z)}\int_{-l}^{l}\int_0^\infty\frac{x-x'}{\rho}k_\rho^2 V_i^h J_1(k_\rho\rho)dk_\rho dy' \quad (12)$$

where $\rho_+ = ((x-x')^2+(y-l)^2)^{1/2}$ and $\rho_- = ((x-x')^2+(y+l)^2)^{1/2}$ are the horizontal distance between the two ends of the line source and the receiver.

III. Fréchet Derivatives

Before inversion, we need to determine the EM responses at the receiver to a small perturbation of the model vector, which is also known as the Fréchet derivatives. We assume that a small perturbation $\delta\sigma_n$ is generated for the conductivity of the nth layer. By substituting this small perturbation into (1) and (2), we can show that the field perturbation caused by this small perturbation satisfies the following equations:

$$\nabla\times\delta\mathbf{E}(\mathbf{r}_r,\mathbf{r}_s) = -j\omega\mu\delta\mathbf{H}(\mathbf{r}_r,\mathbf{r}_s) \quad (13)$$

$$\nabla\times\delta\mathbf{H}(\mathbf{r}_r,\mathbf{r}_s) = j\omega\tilde{\varepsilon}\delta\mathbf{E}(\mathbf{r}_r,\mathbf{r}_s)+\mathbf{J}'(\mathbf{r}) \quad (14)$$

where $\mathbf{J}'(\mathbf{r}) = \delta\sigma_n\mathbf{E}(\mathbf{r},\mathbf{r}_s)$ is defined as the equivalent source, $\mathbf{r}_r$ and $\mathbf{r}_s$ indicate the locations of the receiver and the source, respectively, and $\mathbf{r}$ represents a position in the perturbed layer.

By using the similar procedure for the derivation of (5) and (6) from (1) and (2), we can obtain the following equations:

$$\delta\tilde{\mathbf{E}}(\mathbf{r}_r,\mathbf{r}_s) = \left\langle\tilde{\mathbf{G}}^{\mathrm{EJ}};\mathbf{J}'\right\rangle \quad (15)$$

$$\delta\tilde{\mathbf{H}}(\mathbf{r}_r,\mathbf{r}_s) = \left\langle\tilde{\mathbf{G}}^{\mathrm{HJ}};\mathbf{J}'\right\rangle. \quad (16)$$

Because of the similarity between (5) and (15), and between (6) and (16), $\delta\tilde{\mathbf{H}}(\mathbf{r}_r,\mathbf{r}_s)$ in (16) is also in the form of Sommerfeld integrals. In the following, only the x-component of $\delta\mathbf{H}^n$, δH_x^n, is given (the detailed formulas of y- and z-components are given in the Appendix). The superscript n means that the value $\delta\mathbf{H}$ at $\mathbf{r}_r$ is produced by the small perturbation in the nth layer

$$\delta H_x^n = F_x^n\delta\sigma_n = \left(F_{x1}^n+F_{x2}^n+F_{x3}^n\right)\delta\sigma_n \quad (17)$$

$$F_{x1}^n = -\frac{J_y}{2\pi}\int_{z_{n-1}}^{z_n}\int_0^{+\infty}\int_{-l}^{+l}I_i^e(z_r,z)V_i^e(z,z_s)\times J_{b1}k_\rho dk_\rho dz dy' \quad (18)$$

$$F_{x2}^n = -\frac{J_y}{2\pi}\int_{z_{n-1}}^{z_n}\int_0^{+\infty}\int_{-l}^{+l}I_i^h(z_r,z)V_i^h(z,z_s)\times J_{b2}k_\rho dk_\rho dz dy' \quad (19)$$

$$F_{x3}^n = -\frac{J_y}{2\pi\omega^2\varepsilon_0^2\varepsilon_z^2}\int_{z_{n-1}}^{z_n}\int_0^{+\infty}\int_{-l}^{+l}I_v^e(z_r,z)I_i^e(z,z_s)\times J_{b1}k_\rho^3 dk_\rho dz dy' \quad (20)$$

where I_v^e (the superscript e means TM fields) is the current at z due to a 1-V series voltage source at z', which is denoted by the subscript v, $\mathbf{F}^n$ is usually called the Fréchet derivative for the conductivity perturbation in the nth layer, J_{bj}, $(j=1,2)$ is a Bessel function term

$$J_{b1} = J_0(k_\rho\rho)\sin^2\theta+\frac{\cos 2\theta}{k_\rho\rho}J_1(k_\rho\rho)$$

$$J_{b2} = J_0(k_\rho\rho)\sin^2\theta-\frac{\cos 2\theta}{k_\rho\rho}J_1(k_\rho\rho) \quad (21)$$

where θ is a function of y', which, however, changes along the source line, and J_y is the current density of the line source.

In (18)–(20), the Fréchet derivative is a triple integral and contains Bessel functions. Therefore, its numerical calculation will be very slow. Fortunately, the integral variables are independent of each other, and thus, we can further simplify the integral in (18)–(20) by applying the same method used to simplify (7)–(9) to (10)–(12). In this way, (18)–(20) become the following form:

$$F_{x1}^n = -\frac{J_y}{2\pi}\frac{y_r-y'_+}{\rho_+}\int_{z_{n-1}}^{z_n}\int_0^\infty I_i^e(z_r,z)V_i^e(z,z_s)\times J_1(k_\rho\rho_+)dk_\rho dz + \frac{J_y}{2\pi}\frac{y_r-y'_-}{\rho_-}\int_{z_{n-1}}^{z_n}\int_0^\infty I_i^e(z_r,z)V_i^e(z,z_s)\times J_1(k_\rho\rho_-)dk_\rho dz \quad (22)$$

$$F_{x2}^n = \frac{J_y}{2\pi}\frac{y_r-y'_+}{\rho_+}\int_{z_{n-1}}^{z_n}\int_0^\infty I_i^h(z_r,z)V_i^h(z,z_s)\times J_1(k_\rho\rho_+)dk_\rho dz - \frac{J_y}{2\pi}\frac{y_r-y'_-}{\rho_-}\int_{z_{n-1}}^{z_n}\int_0^\infty I_i^h(z_r,z)V_i^h(z,z_s)\times J_1(k_\rho\rho_-)dk_\rho dz$$

$$-\frac{J_y}{2\pi}\int_{z_{n-1}}^{z_n}\int_0^{\infty}\int_{-l}^{+l} k_\rho I_i^h(z_r,z)V_i^h(z,z_s) \times J_0(k_\rho\rho)dy'dk_\rho dz \quad (23)$$

$$F_{x3}^n = -\frac{J_y}{2\pi\omega^2\varepsilon_0^2\varepsilon_z^2}\frac{y_r-y'_+}{\rho_+}\int_{z_{n-1}}^{z_n}\int_0^{\infty} k_\rho^2 I_v^e(z_r,z)I_i^e(z,z_s) \times J_1(k_\rho\rho_+)dk_\rho dz + \frac{J_y}{2\pi\omega^2\varepsilon_0^2\varepsilon_z^2}\frac{y_r-y'_-}{\rho_-}\int_{z_{n-1}}^{z_n}\int_0^{\infty} k_\rho^2 I_v^e(z_r,z)I_i^e(z,z_s) \times J_1(k_\rho\rho_-)dk_\rho dz \quad (24)$$

where y'_- and y'_+ represent the y coordinates of the starting point and end point of the line source, and y_r represents the y coordinate of the receiver. Note that the variable z is only contained in the current term I or voltage term V of the integrand in (22)–(24). Therefore, we can further simplify them by computing the integral with respect to z analytically. According to the transmission-line formalism, $V(z,z_s)$ is readily determined as [33]

$$V(z,z_s) = V_{ms}(z_{ms})\frac{\prod_{k=ms}^{z_{n-2}}\vec{T}_k^p}{1+\vec{\Gamma}_{z_n}^p t_{z_n}^p} \times[1+\vec{\Gamma}_{z_n}^p e^{-j2k_{z_n}^p(z_n-z)}]e^{-jk_{z_{n-1}}^p(z-z_{n-1})} \quad (25)$$

where ms denotes the layer in which the source is located. In this paper, the source is located on the ground surface, so $ms = 0$. The voltages and currents have reciprocity properties [33]

$$\begin{aligned} V_i(z|z') &= V_i(z'|z) \\ I_v(z|z') &= I_v(z'|z) \\ V_v(z|z') &= -I_i(z'|z). \end{aligned} \quad (26)$$

Using the reciprocity properties, we can rewrite $I_i^e(z_r,z)V_i^e(z,z_s)$ of (22) as

$$V(z,z_r)V(z,z_s) = V_{mr}(z_{mr})V_{ms}(z_{ms}) \times\frac{\prod_{k=mr}^{z_{n-2}}\vec{T}_k^p}{1+\vec{\Gamma}_{z_n}^p t_{z_n}^p}\frac{\prod_{k=ms}^{z_{n-2}}\vec{T}_k^p}{1+\vec{\Gamma}_{z_n}^p t_{z_n}^p}\cdot P(z) \quad (27)$$

where $P(z)$ is defined as

$$\begin{aligned} P(z) = {} & e^{-jk_n^p 2(z-z_n)} + \vec{\Gamma}_{z_n}^p e^{-jk_{z_n}^p(2z_{n+1}-2z_n)} \\ & + \vec{\Gamma}_{zl2}^p e^{-jk_{z_n}^p(2z_{n+1}-2z_n)} \\ & + \vec{\Gamma}_{z_n}^p\vec{\Gamma}_{z_n}^p e^{-jk_{z_n}^p 2(2z_{n+1}-z-z_n)}. \end{aligned} \quad (28)$$

Because only $P(z)$ is related to the variable z in (27), $\int_{z_n}^{z_{n+1}} V(z,z_r)V(z,z_s)dz$ can be rewritten as

$$\int_{z_n}^{z_{n+1}} V(z,z_r)V(z,z_s)dz = V_{mr}(z_{mr})V_{ms}(z_{ms})\frac{\prod_{k=mr}^{z_{n-2}}\vec{T}_k^p}{1+\vec{\Gamma}_{z_n}^p t_{z_n}^p}\frac{\prod_{k=ms}^{z_{n-2}}\vec{T}_k^p}{1+\vec{\Gamma}_{z_n}^p t_{z_n}^p}\cdot\int_{z_n}^{z_{n+1}} P(z)dz. \quad (29)$$

It is easy to show that

$$\int_{z_n}^{z_{n+1}} P(z)dz = \left[\vec{\Gamma}_{z_n}^p e^{-jk_{z_n}^p(2z_{n+1}-2z_n)} + \vec{\Gamma}_{zl2}^p e^{-jk_{z_n}^p(2z_{n+1}-2z_n)}\right](z_n-z_{n-1}) - \frac{1}{2jk_{z_n}^p}e^{-jk_{z_n}^p 2(z_{n+1}-z_n)} + \frac{1}{2jk_{z_n}^p} - \frac{1}{2jk_{z_n}^p}e^{-jk_{z_n}^p 2(z_{n+1}-z_n)} + \frac{1}{2jk_{z_n}^p}e^{-jk_{z_n}^p 4(z_{n+1}-z_n)}. \quad (30)$$

The derivation procedures for $\int_{z_n}^{z_{n+1}} I_i^h(z_r,z)V_i^h(z,z_s)dz$ and $\int_{z_n}^{z_{n+1}} I_v^e(z_r,z)I_i^e(z,z_s)dz$ are similar and not presented here.

IV. Inversion

In the inverse procedure, we assume that the layer thickness, permittivity, and permeability are known, and retrieve the conductivity in each layer from the measured fields at the receivers. Several methods have been proposed for the inversion procedure, such as distorted Born approximation [34], modified quasi-linear approximation [35], Born and Rytov approximations [36], distorted Born iterative method (DBIM) [37]–[39], and so on. For most of these methods, the nonlinear problem of minimization of the cost function is linearized in the inverse iteration process. In DBIM, the distorted Born approximation is used for linearization and Green's functions are updated in each iteration [34]. It is one of the optimization techniques for minimizing the cost-function and has a faster convergence rate than the Born iterative method [40]. The cost function in DBIM is defined as

$$C_{n+1}(\delta\vec{\sigma}_{m+1}) = \frac{\|\delta\mathbf{f}-\mathbf{F}\cdot\delta\vec{\sigma}_{m+1}\|^2}{\|\mathbf{f}^{\text{obs}}\|^2} + \gamma^2\frac{\|\delta\vec{\sigma}_{m+1}\|^2}{\|\vec{\sigma}_m\|^2} \quad (31)$$

where $\|\cdot\|$ denotes the L2-norm, $\delta\mathbf{f}$ denotes the error between the measured field and the predicted field, $\mathbf{F}$ denotes the Fréchet derivative matrix, $\mathbf{F}\cdot\delta\vec{\sigma}_{m+1}$ is the field value caused by the conductivity σ update, and γ^2 is the regularization factor. Previous research shows that it can be chosen as $\gamma^2 = \max\{10^{-\text{SNR(dB)}/5}, 10^{-6}\}$, where SNR(dB) is the signal-to-noise ratio (SNR) of the measurement in decibels [41]. However, for the DBIM inversion applied to our 1-D layered model, numerical experiments show that 0.01 is a better choice for γ^2 (or 0.1 for γ) when the layer number is equal to or larger than 10. $\vec{\sigma}_m$ is the vector of inversion parameters in the mth iteration, $\mathbf{f}^{\text{obs}}$ represents the measured data, and the second term in the right-hand side of (31) is the regularization term. This well-studied linear least square problem is equivalent to solving the following equation [37]:

$$\left(\frac{\mathbf{F}^\dagger\mathbf{F}}{\|\mathbf{f}^{\text{obs}}\|^2} + \frac{\gamma^2}{\|\vec{\sigma}_m\|^2}\mathbf{I}\right)\delta\vec{\sigma}_{m+1} = \frac{\mathbf{F}^\dagger\delta\mathbf{f}}{\|\mathbf{f}^{\text{obs}}\|^2} \quad (32)$$

where $\mathbf{F}^\dagger$ is the conjugate transpose of $\mathbf{F}$. In this paper, the SVD method is applied to solve (32). In each iteration, once $\delta\vec{\sigma}_{m+1}$ is solved from (32), σ is updated immediately. Then, we can recalculate the magnetic fields in the forward model and update Fréchet derivative $\mathbf{F}$ using this new σ. Then, we substitute the updated $\delta\mathbf{f}$ and $\mathbf{F}$ into (32) and solve next $\delta\vec{\sigma}_{m+2}$ again. This iteration continues until the convergence condition is satisfied, i.e., $(\|\delta\mathbf{f}\|/\|\mathbf{f}^{\text{obs}}\|)$ is smaller than a prescribed threshold. Fig. 2 shows the flowchart of the inverse procedure.

V. Numerical Validation

In this section, we first demonstrate the validity of the forward model and Fréchet derivatives, and then present the inversion results and discuss the precision and robustness of the above DBIM inversion algorithm.

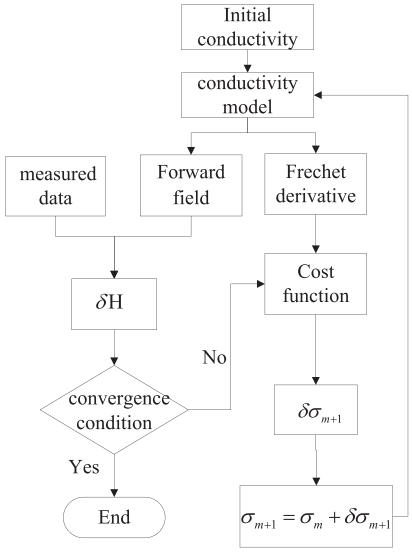

Fig. 2. Flowchart of the inverse procedure.

A. Forward Modeling Validation

We assume that the first model only has three layers. The first layer is air; the thickness of second layer is 200 m and the conductivity is 0.2 S/m; the third layer extends downward to infinity and the conductivity is 0.01 S/m. The line source is located at the ground surface along the y-direction in the range of 0–2000 m. Totally, 201 observers evenly distribute in the range of $(-2000, 300, -125)$ to $(2000, 300, -125)$ m. All the observers are placed in the air and their footprints are in a straight line orthogonal to the line source. In order to verify the semianalytical formulas given in (10)–(12) for the computation of magnetic fields excited by a line source in a layered medium, we compare the magnetic field calculated by (10)–(12) to those computed by Gauss integral methods. The 2000-m-long line source is divided into 20 sections and we apply the Gauss integral of 32 points to each section. Fig. 3 displays the comparisons of x-component H-fields between the Gauss integral results and semianalytical results from (10). The relative error between the results of two methods is defined as

$$\text{err} = \frac{\|\mathbf{H}^s - \mathbf{H}^g\|}{\|\mathbf{H}^g\|} \tag{33}$$

where $\|\cdot\|$ denotes the L2-norm, and $\mathbf{H}^g$ and $\mathbf{H}^s$ represent the Gauss integral results and semianalytic results, respectively. The magnetic field computed by the semianalytical method fits well with the Gauss integral result. The relative error of the two methods is $\text{err} = 9.74 \times 10^{-7}$.

B. Validation of Fréchet Derivatives

We use the finite-difference (FD) algorithm given in [42] to verify the Fréchet derivatives. The basic idea of the FD method is to compute the field value change caused by an infinitesimal model parameter perturbation (e.g., the conductivity σ changes in a certain layer) [30], [42], [43]. Here, we use the same parameters of the layered model, the line source, and the observation points as those in Section V-A, and assume that the small perturbation occurs in the second layer. Fig. 4 shows that the semianalytical results computed by (17) match the

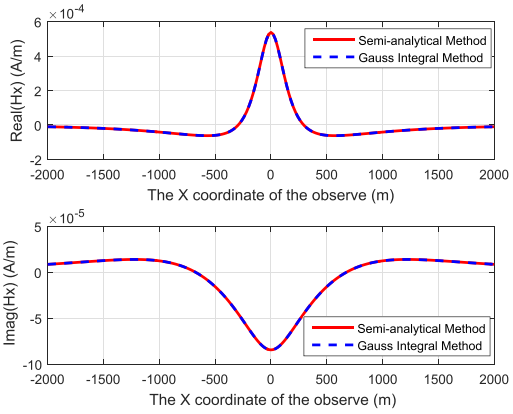

Fig. 3. Comparisons of the x-component of the H-field between semianalytical results and Gauss integral results. (Top) Real part of the x-component of H-fields. (Bottom) Imaginary part of the x-component of H-fields.

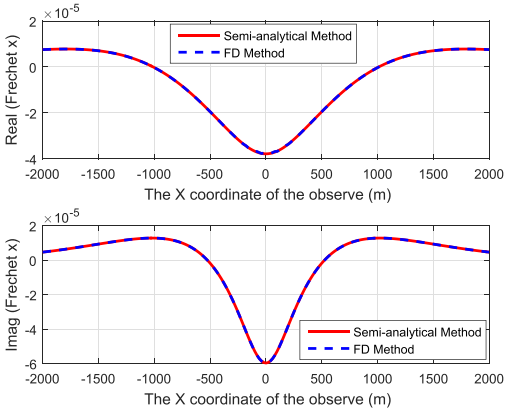

Fig. 4. Comparisons of the x-component of the Fréchet derivative between semianalytical results and FD results. (Top) Real part of the x-component of the Fréchet derivative. (Bottom) Imaginary part of the x-component of the Fréchet derivative.

FD method results well. The relative error between the results of two methods is defined as

$$\text{err} = \frac{\|\mathbf{F}^s - \mathbf{F}^{\text{FD}}\|}{\|\mathbf{F}^{\text{FD}}\|} \tag{34}$$

where $\|\cdot\|$ denotes the L2-norm, and $\mathbf{F}^s$ and $\mathbf{F}^{\text{FD}}$ are the semianalytical results and FD results, respectively. The relative error of the two methods is $\text{err} = 1.02\%$.

C. Inversion Validation

We apply the inversion algorithm to three models to verify its correctness. In the first model, there are five layers. The first layer is air; the thicknesses of the middle three layers are 50, 200, and 200 m, respectively, and the conductivities are 0.005, 0.01, and 0.2 S/m, respectively; the last layer extends downward to infinity and the conductivity is 0.02 S/m. The second model is constructed by uniformly dividing the middle three layers in the first model into two layers, respectively, and adding one extra layer to its last layer at the bottom. Therefore, there are totally nine layers in the second model, and the thicknesses of the seven middle layers are 25, 25, 100, 100, 100, 100, 100 m, respectively. The last layer at the bottom also

extends downward to infinity. The conductivity at any depth in the second model keeps the same as that at the same depth in the first model. Similarly, the third model is constructed by dividing the middle three layers in the first model into three layers, respectively, and adding two extra layers to its last layer at the bottom. Therefore, there are totally 13 layers in the third model and the thicknesses of the 11 middle layers are 17.5, 17.5, 15, 60, 60, 80, 60, 60, 80, 60, 60 m, respectively. The last layer also extends downward to infinity. The conductivity at any depth in the third model keeps the same as that at the same depth in the first model. The line source is located on the ground surface along the y-direction in the range of 0–2000 m in all the three models. We assume that there is only one receiver in the air located at $(50, 800, -125)$ m.

In a conductive medium, the wave amplitude roughly decays exponentially. Higher frequency components have a smaller penetration depth. Therefore, we sample the magnetic field data at the receivers in an exponential way, i.e., the sampling points in the frequency axis are determined by uniformly dividing the logarithm of the starting point and the ending point of the frequency. For example, in the current validation, we choose 30 frequency points between 10 and 500 Hz. Three components of the magnetic field are employed in the inversion for all three models.

At the beginning of the iteration, it is assumed that the underground is homogeneous and the conductivity is a randomly selected value of 0.02 S/m. The prescribed threshold of the magnetic field relative error is 0.1%. The regularization factor γ values for the first and second models are set to be 0.001 according to [41] but 0.1 for the third model, since there are totally 13 layers. The iteration will also stop if the number of iterations reaches 16. The inversion results without noise are shown in Fig. 5. From the result for the first model, we can see that the conductivity in all layers can be accurately retrieved. In model 2 and model 3, the final inversion results keep close to the real values although some errors show up. Therefore, in all the three models, the retrieved conductivity values are close to the real values, although the initial value is a random guess. We also tested other initial values, but the inversion results are kept the same. This means that our inversion method weakly depends on the initial guess.

Now, let us verify the noise tolerance of our inversion algorithm. The noise data have the additive white Gaussian model and are defined by $H_n(i) = H(i)(1 + \varepsilon_{ns} N(i))$ [30], where the subscript n represents the data after adding noise, i represents the magnetic field data at the ith frequency, $H(i)$ represents the H-field without noise, $N(i)$ represents a series of random numbers in the range of $[-1, 1]$, and the amplitude of the noise is expressed by ε_{ns}. We use the same layer and conductivity distribution as in the first model. The initial conductivity is also 0.02 S/m for all the three models. The γ values for these three models are 0.001, 0.01, and 0.1, respectively. The stopping criterion of the iteration is the same as that of the first model. The inversion results with 40, 20, and 10 dB SNR are given in Fig. 6. We observe that the retrieved conductivities are consistent with the model parameters in most layers. The relative errors of the H-field for noisy data with SNR = 40, 20, and 10 dB in each iteration are shown in Fig. 7. The results demonstrate that the convergence errors drop rapidly in the first several iterations, and then,

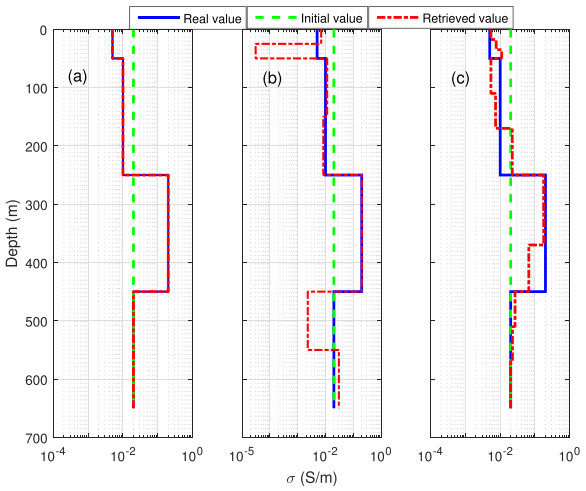

Fig. 5. Comparisons of inversion results without noise. (a) First model. (b) Second model. (c) Third model.

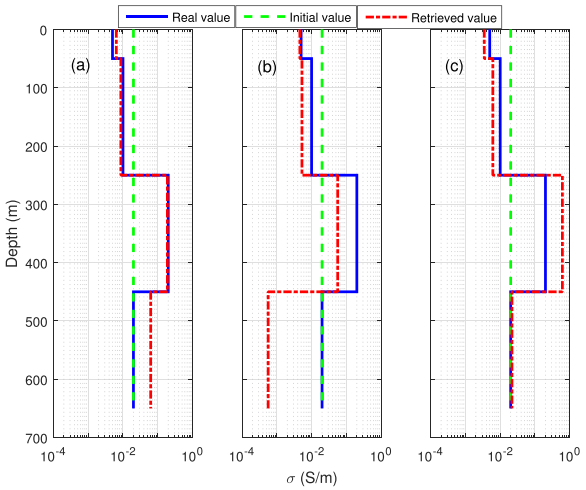

Fig. 6. Comparisons among the initial model, the true model, and inversion results for input data with white Gaussian noise. (a) SNR = 40 dB. (b) SNR = 20 dB. (c) SNR = 10 dB.

they gradually converge. In order to quantitatively determine the inversion error, we define the estimation error between the retrieved conductivity and the real value as

$$E_{\text{err}} = \frac{\|\sigma^{\text{retrieved}} - \sigma^{\text{real}}\|}{\|\sigma^{\text{real}}\|} \tag{35}$$

where $\|\cdot\|$ denotes the L2-norm, and $\sigma^{\text{retrieved}}$ and σ^{real} are the retrieved and real conductivity values, respectively. Since the first layer in all the models is air, its conductivity value is not included in both $\sigma^{\text{retrieved}}$ and σ^{real}. Fig. 8 shows the relative errors of the H-field when the iterations converge and the estimation errors for different SNR values ranging from 10 to 40 dB with the step of 5 dB. The results indicate that the convergence relative error is roughly at the same level of the noise when the iteration converges. However, the estimation errors show some fluctuation although the general trend is descending. The retrieved conductivity is also affected by the noise and its value in a certain layer may deviate a little far away from the real value and this will cause the sudden increase of the estimation error, e.g., when

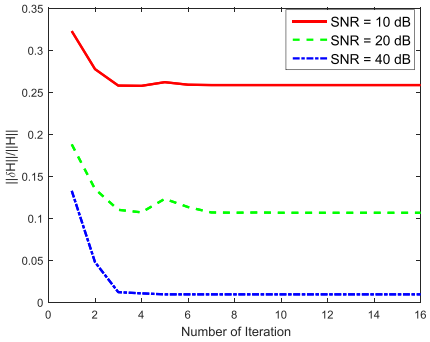

Fig. 7. Relative errors of the magnetic fields in each iteration for the inversion in Fig. 5.

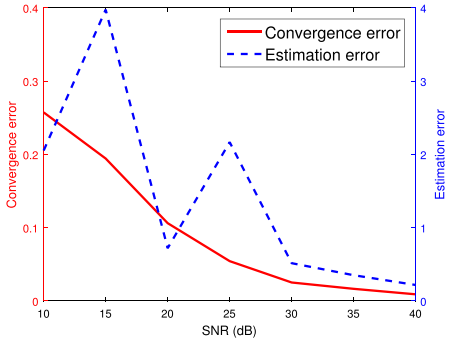

Fig. 8. Relative errors when the iteration converges and estimation errors versus SNR.

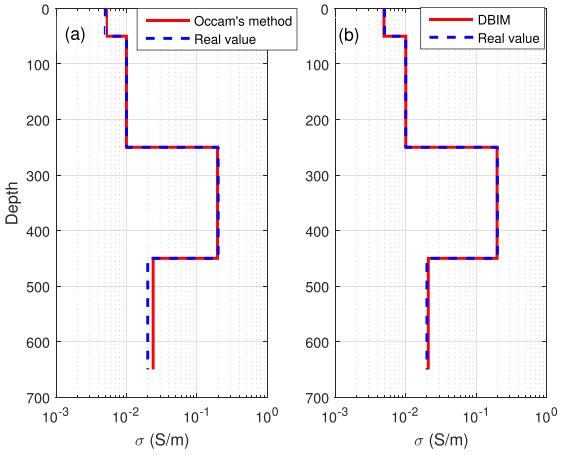

Fig. 9. Inversion results of the first model. (a) Occam's inversion. (b) DBIM's inversion.

SNR = 15 or 25 dB. From the above comparisons, we can see that our inversion algorithm has a certain antinoise ability.

Finally, we want to emphasize that our DBIM inversion algorithm may be improved further by combining with other multifrequency method such as iterative multiresolution approaches and the frequency-hopping method [44]–[46], which have been applied in ground penetrating radar detection in the subsurface region. However, this will be left as a topic for our future research.

D. Comparison With Occam's Inversion

In order to evaluate our method's computational accuracy and efficiency, we compare the DBIM algorithm with the open-source Occam's code[1] given by the Scripps Institution of Oceanography, University of California San Diego, San Diego, CA, USA [47]. Here, we use the same layer configurations and synthetic data as those in the first model and the third model in Section V-C. The only difference in the following comparisons is that a dipole source is used instead of a line source, since the line source is obtained by integrating the dipole source. For the first model, we choose the initial conductivity 0.02 S/m and γ 0.001 for our DBIM method, and the reconstructed results are shown in Fig. 9. The two methods use the same synthetic data for 1 receiver and 20 frequencies. In a personal computer with the CPU of Intel Core i5-2400 3.10 GHz, Occam's inversion and DBIM inversion take 1.21 and 0.96 s CPU time, respectively. The DBIM algorithm requires five iterations, but Occam's inversion requires 12. The estimation error defined by (35) between the retrieved value and the real value is 3.43% for Occam's inversion but only 1.08% for the DBIM algorithm. For the third model, we choose the initial conductivity 0.02 S/m and γ 0.1 for our DBIM method, and the reconstructed results are shown in Fig. 10. We also use the data for one receiver but increase the frequency number to 30, since the layer number increases, and thus the unknowns also increase. Occam's inversion and the DBIM algorithm take 7.04 and 9.78 s CPU time, respectively. The estimation errors of Occam's inversion and the DBIM are 31.84% and 22.74%, respectively. From these comparisons, we know that the computation time of Occam's inversion and the DBIM has no big difference although the later one takes less iteration steps. Our DBIM method outperforms a little than Occam's inversion for the estimation error. Occam's inversion algorithm uses the parameterized model and the minimum norm solution yields the smoothest possible model [23]. Its inversion fits the data while enforcing smoothness [8]. However, the DBIM algorithm is an optimization technique for minimizing the cost-function. Therefore, Occam's inversion algorithm usually yields a smoother result than the DBIM algorithm, especially when the layer number is large.

VI. Inversion for Measured Data

A new GREATEM system has been developed [48]. The system is composed of an unmanned aerial vehicle (UAV), a grounded-wire source of 2–3 km in length as the transmitter, and a three-axis induction coil sensor in the towed bird as the detector. A global positioning system (GPS) and a gyroscope are placed on the UAV. The line source on the ground is fed by a bipolar square pulse current. The receivers in the UAV record the magnetic fields, which include both the direct wave and the ground response of the pulsed current. The whole system is synchronized by the GPS time. A GPS measurement is used to determine the position and height of the moving receivers. The height of the receivers above the ground ranges from 100 to 150 m in surveys.

An area in Changyi City, Shandong province, China, was surveyed in January 2016. A 2768-m transmitter cable was

[1]The open-source Occam's inversion code is downloaded from http://marineemlab.ucsd.edu/Projects/Occam/1DCSEM/index.html.

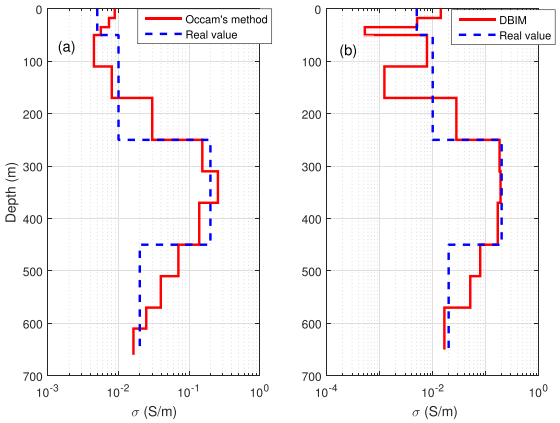

Fig. 10. Inversion results of the third model. (a) Occam's inversion. (b) DBIM's inversion.

Fig. 11. Satellite map of survey area at Changyi. Black line: flight path. Red line: grounded-wire source.

placed from west to east, as shown in Fig. 11. The speed of flights was about 60 km/h. The waveform has a period of 80 ms and a duty cycle of 50%. The high current is 20 A, while the low current is −20 A, as shown in Fig. 12(a). The turn-ON (rising from 0 to ±20 A) time is about 80 μs and the turn-OFF (dropping from ±20 to 0 A) time is about 4 μs. Full time-series raw data of the three components of the magnetic fields were recorded in the format of voltage, as shown in Fig. 12(b)–(d).

The data preprocessing include the following steps.

1) *Angle Correction:* During the GREATEM survey, both the flight acceleration and the wind direction can change the posture of the receiver coil, which leads to the deviation of the local coordinate of the three orthogonal magnetic sensors away from the coordinate in our inversion algorithm. Therefore, it is necessary to correct the angle of the data. The correction is made using a triaxis orthogonal coordinate transformation based on the gyroscope data.
2) *System Noise Removal:* Experiments are conducted in suburban open fields far away from the downtown of Changyi City. Noises from the clutter, such as the terrains or instruments themselves, are not considered. However, magnetic field data include other kinds of noise, such as Sferic noise, powerline noise, and so on. As shown in Fig. 12(b)–(d), there are slow varying signals existing in the raw data and four rising edges

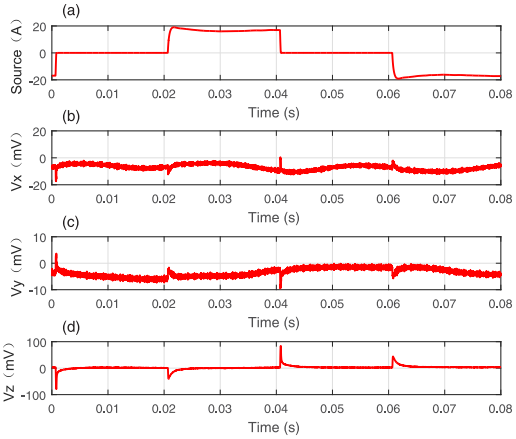

Fig. 12. Example of the source waveform in the time domain and the raw voltage signals recorded by three orthogonal magnetic coils. (a) Source current waveform. (b) x component of raw voltage signal. (c) y component of raw voltage signal. (d) z component of raw voltage signal.

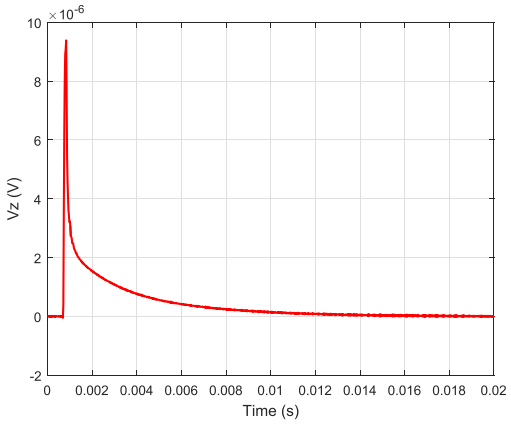

Fig. 13. z-component of a typical turn-OFF signal after preprocessing.

(included in both the positive and negative pulses) in each cycle. The signal can be considered zero before the rising edge, because it has been attenuated small enough. Therefore, we pick four data values before four rising edges, respectively, and fit them with a quadratic curve. The curve data are treated as slow varying system noise and removed by subtracting them from the concurrent airborne data.

3) *Data Stacking:* The random noise is the inevitable interference to all systems and is distributed in all parts of the data. Data stacking is the most effective way to remove the random noise. As the data period is 0.08 s, we stack the data of 50 cycles (4-s data). A typical turn-OFF signal after preprocessing is shown in Fig. 13. In the next step, we transform the data from the time domain to the frequency domain. The spectrum of the turn-OFF signal shown in Fig. 13 is illustrated in Fig. 14. We select a series of frequency points for inversion. They are ranged from 10 to 500 Hz and sampled in exponential intervals. There is no aliasing, since the sampling frequency of the raw data is 48 K.

As shown in Fig. 11, there are 14 flight lines. Here, we take line E as an example. The flight speed of UAV is

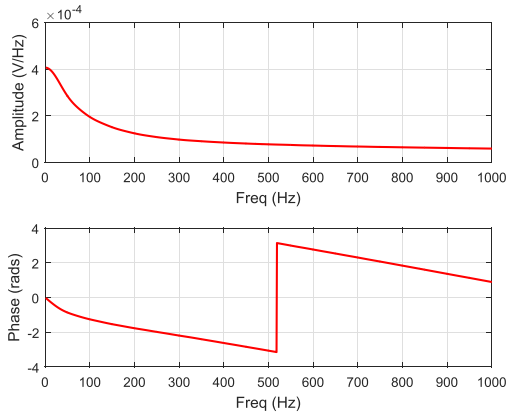

Fig. 14. Signal shown in Fig. 9 is transformed into frequency domain.

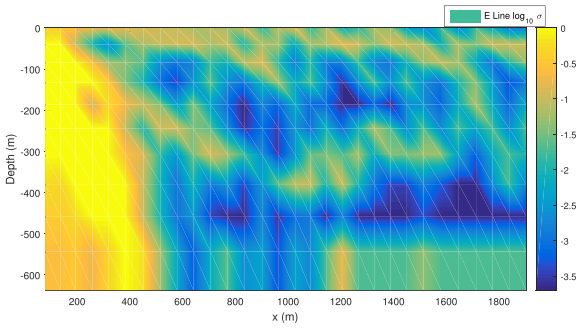

Fig. 15. Logarithm of the conductivity section along the flight line E.

60 km/h, and the flight distance is about 60 m in 4 s. The length of E line is about 1800 m. Therefore, the E line can be divided into 30 sections and each section has the length of 60 m. Due to the slow variation of conductivity distribution, we assume that the conductivity inside each section is laterally homogeneous. Combining the 1-D inversion result of the 30 sections, we obtain a 2-D conductivity distribution. Fig. 15 shows the retrieved 2-D electrical conductivity profile along line E. There is a layer of high conductivity at the depth less than 50 m. There are also some bands of high conductivity area between 200 and 300 m. The retrieved conductivity near the source (at $x = 0$ m) is usually not reliable, since the noise coupled from the transmitter is strong and the transient ground response attenuates rapidly to less than the noise level [10], [13]. According to the existing drilling data, the surface of the detected area is quaternary, followed by shale; at 200 and 300 m depth, there is a strip of iron ore, followed by a granite layer beneath it. Therefore, the inversion results from our algorithm are roughly consistent with the existing data. Fig. 16 shows the initial error at the beginning of the iterations and the convergence error when iterations finish. We can see that the relative error of the H-field converges to a lower level than the initial error in the whole receiver line.

VII. Conclusion

In this paper, a new iterative inversion algorithm for GREATEM data has been established to reconstruct the conductivity profile in the stratified underground. The mathematical expressions of both the magnetic field in forward modeling and the Fréchet derivative for the EM response to the model perturbation are simplified to save the computation cost. Numerical experiments show that not only the forward modeling and Fréchet derivative are efficient and accurate, but also the inversion method is reliable and robust under noise contamination. We compare our DBIM method to the open-source Occam's method and find that the computation accuracy of DBIM is a little higher than that of Occam's method. There is no big difference of the computation time-consumption between two methods. Occam's method can yield a smoother profile than the DBIM method when the layer number is large. By applying our inversion algorithm to the measured data collected by the new GREATEM system, we find that the retrieved conductivity distribution under the surveyed area is roughly consistent with the drilling data. Therefore, this proposed inversion algorithm for GREATEM can be a choice in practical engineering for mineral detection, groundwater location, and other subsurface imaging applications.

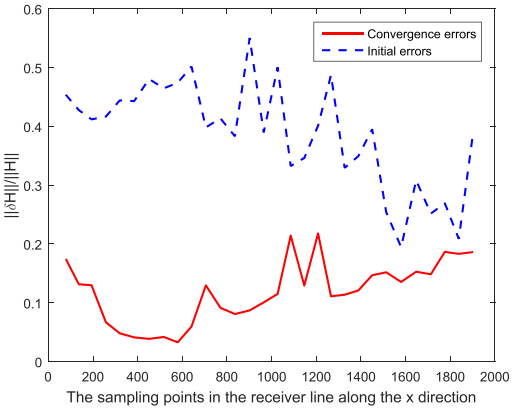

Fig. 16. Convergence errors along the flight line E.

Appendix
Fréchet Derivative

The y- and z-components of the Fréchet derivatives are as follows:

$$\delta H_y^n = F_y^n \delta\sigma_n = \left(F_{y1}^n + F_{y2}^n + F_{y3}^n\right)\delta\sigma_n \tag{36}$$

$$F_{y1}^n = \frac{J_y}{4\pi}\int_{z_{n-1}}^{z_n}\int_0^{+\infty}\int_{-l}^{+l} I_i^e(z_r,z)V_i^e(z,z_s)\sin 2\theta \times J_{b3}k_\rho dk_\rho dz dy' \tag{37}$$

$$F_{y2}^n = -\frac{J_y}{4\pi}\int_{z_{n-1}}^{z_n}\int_0^{+\infty}\int_{-l}^{+l} I_i^h(z_r,z)V_i^h(z,z_s)\sin 2\theta \times J_{b3}k_\rho dk_\rho dz dy' \tag{38}$$

$$F_{y3}^n = \frac{J_y}{4\pi\omega^2\varepsilon_0^2\varepsilon_z^2}\int_{z_{n-1}}^{z_n}\int_0^{+\infty}\int_{-l}^{+l} I_v^e(z_r,z)I_i^e(z,z_s) \times \sin 2\theta J_{b3}k_\rho^3 dk_\rho dz dy' \tag{39}$$

$$\delta H_z^n = F_z^n \delta\sigma_n \tag{40}$$

$$F_z^n = -\frac{jJ_y}{2\pi\omega\mu_0\mu'}\int_{z_{n-1}}^{z_n}\int_0^{\infty}\int_{-l}^{+l} V_i^h(z,z_r)V_i^h(z,z_s) \times \cos\theta J_1(k_\rho\rho)dk_\rho dz dy' \tag{41}$$

where $J_{bj}(j = 1, 2, 3)$ is a Bessel function term, and J_y is the current density of the line source. The detailed formula of J_{bj} for δH^n is as follows:

$$J_{b1} = J_0(k_\rho \rho)\sin^2\theta + \frac{\cos 2\theta}{k_\rho \rho} J_1(k_\rho \rho)$$

$$J_{b2} = J_0(k_\rho \rho)\sin^2\theta - \frac{\cos 2\theta}{k_\rho \rho} J_1(k_\rho \rho)$$

$$J_{b3} = J_0(k_\rho \rho) - \frac{2}{k_\rho \rho} J_1(k_\rho \rho). \quad (42)$$

REFERENCES

[1] D. Fountain, "Airborne electromagnetic systems—50 years of development," *Exploration Geophys.*, vol. 29, nos. 1–2, pp. 1–11, 1998.

[2] D. Sattel, "A brief discussion of helicopter time-domain electromagnetic systems," in *Proc. SEG Tech. Program Expanded Abstracts Soc. Exploration Geophys.*, 2006, pp. 1268–1272.

[3] D. Sattel, "An overview of helicopter time-domain EM systems," *ASEG Extended Abstracts*, vol. 2009, no. 1, pp. 1–6, Jan. 2009.

[4] R. Smith, "Electromagnetic induction methods in mining geophysics from 2008 to 2012," *Surv. Geophys.*, vol. 35, no. 1, pp. 123–156, 2014.

[5] R. Smith, "Airborne electromagnetic methods: Applications to minerals, water and hydrocarbon exploration," *CSEG Recorder*, vol. 35, no. 3, pp. 7–10, 2010.

[6] G.-Q. Xue, K.-Z. Qin, X. Li, G.-M. Li, Z.-P. Qi, and N.-N. Zhou, "Discovery of a large-scale porphyry molybdenum deposit in Tibet through a modified TEM exploration method," *J. Environ. Eng. Geophys.*, vol. 17, no. 1, pp. 19–25, 2012.

[7] K. Witherly, "The quest for the holy grail in mining geophysics: A review of the development and application of airborne em systems over the last 50 years," *Lead. Edge*, vol. 19, no. 3, pp. 270–274, 2000.

[8] C.-C. Yin, X.-Y. Ren, Y.-H. Liu, Y.-F. Qi, C.-K. Qiu, and J. Cai, "Review on airborne electromagnetic inverse theory and applications," *Geophysics*, vol. 80, no. 4, pp. W17–W31, 2015.

[9] H. Sun, X. Li, S. Li, Z. Qi, M. Su, and Y. Xue, "Multi-component and multi-array TEM detection in karst tunnels," *J. Geophys. Eng.*, vol. 9, no. 4, p. 359, 2012.

[10] T. Mogi *et al.*, "Grounded electrical-source airborne transient electromagnetic (GREATEM) survey of Mount Bandai, north-eastern Japan," *Exploration Geophys.*, vol. 40, no. 1, pp. 1–7, 2009.

[11] X. Wang *et al.*, "Crust and upper mantle resistivity structure at middle section of Longmenshan, eastern Tibetan plateau," *Tectonophysics*, vols. 619–620, pp. 143–148, Apr. 2014.

[12] T. Mogi, Y. Tanaka, K. Kusunoki, T. Morikawa, and N. Jomori, "Development of grounded electrical source airborne transient EM (GREATEM)," *Exploration Geophys.*, vol. 29, no. 2, pp. 61–64, 1998.

[13] H. Ito *et al.*, "Further investigations of underground resistivity structures in coastal areas using grounded-source airborne electromagnetics," *Earth Planets Space*, vol. 63, no. 8, pp. e9–e12, 2011.

[14] H. Ito, H. Kaieda, T. Mogi, A. Jomori, and Y. Yuuki, "Grounded electrical-source airborne transient electromagnetics (GREATEM) survey of Aso Volcano, Japan," *Exploration Geophys.*, vol. 45, no. 1, pp. 43–48, 2014.

[15] X. Wang *et al.*, "Mapping deeply buried karst cavities using controlled-source audio magnetotellurics: A case history of a tunnel investigation in southwest China," *Geophysics*, vol. 82, no. 1, pp. EN1–EN11, 2017.

[16] D. C. Fraser, "Resistivity mapping with an airborne multicoil electromagnetic system," *Geophysics*, vol. 43, no. 1, pp. 144–172, 1978.

[17] H. Huang and D. C. Fraser, "The differential parameter method for multifrequency airborne resistivity mapping," *Geophysics*, vol. 61, no. 1, pp. 100–109, 1996.

[18] R. Schaa and P. K. Fullagar, "Rapid, approximate 3D inversion of transient electromagnetic (TEM) data," in *Proc. SEG Tech. Program Expanded Abstracts, Soc. Exploration Geophys.*, 2010, pp. 650–654.

[19] H. Huang and D. C. Fraser, "Inversion of helicopter electromagnetic data to a magnetic conductive layered earth," *Geophysics*, vol. 68, no. 4, pp. 1211–1223, 2003.

[20] H. Huang and J. Rudd, "Conductivity-depth imaging of helicopter-borne TEM data based on a pseudolayer half-space model," *Geophysics*, vol. 73, no. 3, pp. F115–F120, 2008.

[21] P. Wolfgram and G. Karlik, "Conductivity-depth transform of GEOTEM data," *Exploration Geophys.*, vol. 26, no. 3, pp. 179–185, 1995.

[22] J. Chen and A. Raiche, "Inverting AEM data using a damped eigenparameter method," *Exploration Geophys.*, vol. 29, no. 2, pp. 128–132, 1998.

[23] S. C. Constable, R. L. Parker, and C. G. Constable, "Occam's inversion: A practical algorithm for generating smooth models from electromagnetic sounding data," *Geophysics*, vol. 52, no. 3, pp. 289–300, 1987.

[24] A. Raiche, "Modelling the time-domain response of AEM systems," *Exploration Geophys.*, vol. 29, no. 2, pp. 103–106, 1998.

[25] J. Guillemoteau, P. Sailhac, and M. Behaegel, "Regularization strategy for the layered inversion of airborne TEM data: Application to VTEM data acquired over the basin of Franceville (Gabon)," *Geophys. Prospecting*, vol. 59, no. 6, pp. 1132–1143, 2011.

[26] D. Sattel, "Inverting airborne electromagnetic (AEM) data with Zohdy's method," *Geophysics*, vol. 70, no. 4, pp. G77–G85, 2005.

[27] M. A. Vallée and R. S. Smith, "Application of Occam's inversion to airborne time-domain electromagnetics," *Lead. Edge*, vol. 28, no. 3, pp. 284–287, 2009.

[28] E. Auken and A. V. Christiansen, "Layered and laterally constrained 2D inversion of resistivity data," *Geophysics*, vol. 69, no. 3, pp. 752–761, 2004.

[29] R. Brodie and M. Sambridge, "Holistically calibrating, processing and inverting frequency domain AEM surveys," *ASEG Extended Abstracts*, vol. 2004, no. 1, pp. 1–4, 2004.

[30] H. Wang, "Adaptive regularization iterative inversion of array multicomponent induction well logging datum in a horizontally stratified inhomogeneous TI formation," *IEEE Trans. Geosci. Remote Sens.*, vol. 49, no. 11, pp. 4483–4492, Nov. 2011.

[31] K. A. Michalski and J. R. Mosig, "Multilayered media Green's functions in integral equation formulations," *IEEE Trans. Antennas Propag.*, vol. 45, no. 3, pp. 508–519, Mar. 1997.

[32] S. Rita and B. Michael, "Electromagnetic fields generated by finite-length wire sources: Comparison with point dipole solutions," *Geophys. Prospecting*, vol. 59, no. 2, pp. 361–374, 2011.

[33] K. A. Michalski, *Electromagnetic Field Computation in Planar Multilayers*. Hoboken, NJ, USA: Wiley, 2005.

[34] W. C. Chew and Q.-H. Liu, "Inversion of induction tool measurements using the distorted Born iterative method and CG-FFHT," *IEEE Trans. Geosci. Remote Sens.*, vol. 32, no. 4, pp. 878–884, Jul. 1994.

[35] C. Zhou and L. Liu, "Radar-diffraction tomography using the modified quasi-linear approximation," *IEEE Trans. Geosci. Remote Sens.*, vol. 38, no. 1, pp. 404–415, Jan. 2000.

[36] T. M. Habashy, R. W. Groom, and B. R. Spies, "Beyond the Born and Rytov approximations: A nonlinear approach to electromagnetic scattering," *J. Geophys. Res*, vol. 98, no. B2, pp. 1759–1775, 1993.

[37] F. Li, Q. H. Liu, and L.-P. Song, "Three-dimensional reconstruction of objects buried in layered media using Born and distorted Born iterative methods," *IEEE Geosci. Remote Sens. Lett.*, vol. 1, no. 2, pp. 107–111, Apr. 2004.

[38] Q.-H. Liu, "Reconstruction of two-dimensional axisymmetric inhomogeneous media," *IEEE Trans. Geosci. Remote Sens.*, vol. 31, no. 3, pp. 587–594, May 1993.

[39] Q.-H. Liu, "Nonlinear inversion of electrode-type resistivity measurements," *IEEE Trans. Geosci. Remote Sens.*, vol. 32, no. 3, pp. 499–507, May 1994.

[40] W. C. Chew and Y. M. Wang, "Reconstruction of two-dimensional permittivity distribution using the distorted Born iterative method," *IEEE Trans. Med. Imag.*, vol. 9, no. 2, pp. 218–225, Jun. 1990.

[41] Y. Fang, J. Dai, Z. Yu, J. Zhou, and Q. H. Liu, "Through-casing hydraulic fracture evaluation by induction logging I: An efficient EM solver for fracture detection," *IEEE Trans. Geosci. Remote Sens.*, vol. 55, no. 2, pp. 1179–1188, Feb. 2017.

[42] H. Wang, H. Tao, J. Yao, and Y. Zhang, "Efficient and reliable simulation of multicomponent induction logging response in horizontally stratified inhomogeneous TI formations by numerical mode matching method," *IEEE Trans. Geosci. Remote Sens.*, vol. 50, no. 9, pp. 3383–3395, Sep. 2012.

[43] S. Yang, J. Wang, J. Zhou, T. Zhu, and H. Wang, "An efficient algorithm of both Fréchet derivative and inversion of MCIL data in a deviated well in a horizontally layered TI formation based on TLM modeling," *IEEE Trans. Geosci. Remote Sens.*, vol. 52, no. 11, pp. 6911–6923, Nov. 2014.

[44] M. Salucci, G. Oliveri, and A. Massa, "GPR prospecting through an inverse-scattering frequency-hopping multifocusing approach," *IEEE Trans. Geosci. Remote Sens.*, vol. 53, no. 12, pp. 6573–6592, Dec. 2015.

[45] M. Salucci, L. Poli, and A. Massa, "Advanced multi-frequency GPR data processing for non-linear deterministic imaging," *Signal Process.*, vol. 132, pp. 306–318, Mar. 2017.
[46] M. Salucci, L. Poli, N. Anselmi, and A. Massa, "Multifrequency particle swarm optimization for enhanced multiresolution GPR microwave imaging," *IEEE Trans. Geosci. Remote Sens.*, vol. 55, no. 3, pp. 1305–1317, Mar. 2017.
[47] K. Kerry, "1D inversion of multicomponent, multifrequency marine CSEM data: Methodology and synthetic studies for resolving thin resistive layers," *Geophysics*, vol. 74, no. 2, pp. F9–F20, 2009.
[48] X. Wu *et al.*, "Contrast test of the transient electromagnetic system (CASTEM) at the Dawangzhuang iron mine in Anhui province," *Chin. J. Geophys.*, vol. 59, no. 12, pp. 4448–4456, 2016.

Bingyang Liang received the B.E. degree in communication engineering from PLA Information Engineering University, Zhengzhou, China, in 2011, and the M.S. degree in electronics and communication engineering from Xiamen University, Xiamen, China, in 2014, where he is currently pursuing the Ph.D. degree.

His research interests include the forward and inversion method of electromagnetics and acoustics, as well as their applications in ATEM and photoacoustic tomography.

Chen Qiu received the B.S. degree in electronic information science and technology and the M.A. degree in theoretical physics from Xiamen University, Xiamen, China, in 2010 and 2013, respectively, where he is currently pursuing the Ph.D. degree.

His research interests include fast 3-D electromagnetic forward and inverse scattering algorithm as well as their applications in ATEM and GPR.

Feng Han received the B.S. degree in electronic science from Beijing Normal University, Beijing, China, in 2003, the M.S. degree in geophysics from Peking University, Beijing, in 2006, and the Ph.D. degree in electrical engineering from Duke University, Durham, NC, USA, in 2011.

He is currently an Assistant Professor with the Institute of Electromagnetics and Acoustics, Xiamen University, Xiamen, China. His research interests include ionosphere remote sensing by radio atmospherics, electromagnetic full-wave inversion by integral equations, reverse time migration image, and the design of an electromagnetic detection system.

Chunhui Zhu received the Ph.D. degree in control science and engineering from the Harbin Institute of Technology, Harbin, China, in 2012.

From 2009 to 2011, she was a Visiting Student with the Electrical Engineering Department, Duke University, Durham, NC, USA. Since 2013, she has been with Xiamen University, Xiamen, China, where she is currently an Assistant Professor with the Department of Electronic Science. Her research interests include fast algorithms for computational electromagnetics and their applications in engineering.

Na Liu received the Ph.D. degree in computational mathematics from the University of Chinese Academy of Sciences, Beijing, China, in 2013.

From 2012 to 2013, she was a Visiting Student with the Department of Electrical and Computer Engineering, Duke University, Durham, NC, USA. From 2013 to 2017, she held a postdoctoral position with Xiamen University, Xiamen, China, where she is currently an Associate Professor with the Institute of Electromagnetics and Acoustics. Her research interests include computational electromagnetics, especially the fast and efficient methods for complex media and their applications in cavities and optical waveguide problems.

Hai Liu (S'11–M'13) received the B.E. and M.E. degrees in civil engineering from Tongji University, Shanghai, China, in 2007 and 2009, respectively, and the Ph.D. degree in environmental studies from Tohoku University, Sendai, Japan, in 2013.

From 2013 to 2014, he was a Research Fellow with the Center for Northeast Asian Studies, Tohoku University. He is currently an Assistant Professor with the Institute of Electromagnetics and Acoustics, Xiamen University, Xiamen, China. His research interests include the development of ground-penetrating radar systems and algorithms for a wide variety of applications, such as nondestructive testing in civil engineering, environmental monitoring, archeological investigation, and lunar exploration.

Fubo Liu, photograph and biography not available at the time of publication.

Guangyou Fang, photograph and biography not available at the time of publication.

Qing Huo Liu (S'88–M'89–SM'94–F'05) received the B.S. and M.S. degrees in physics from Xiamen University, Xiamen, China, in 1983 and 1986, respectively, and the Ph.D. degree in electrical engineering from the University of Illinois at Urbana–Champaign, Champaign, IL, USA, in 1989.

From 1986 to 1988, he was a Research Assistant with the Electromagnetics Laboratory, University of Illinois at Urbana–Champaign, where he was a Post-Doctoral Research Associate from 1989 to 1990. He was a Research Scientist and the Program Leader with Schlumberger-Doll Research, Ridgefield, CT, USA, from 1990 to 1995. From 1996 to 1999, he was an Associate Professor with New Mexico State University, Las Cruces, NM, USA. Since 1999, he has been with Duke University, Durham, NC, USA, where he is currently a Professor of electrical and computer engineering. He has authored over 400 papers in refereed journals and 500 papers in conference proceedings. His research interests include computational electromagnetics and acoustics, inverse problems, and their applications in nanophotonics, geophysics, biomedical imaging, and electronic packaging.

Dr. Liu is a fellow of the Acoustical Society of America, the Electromagnetics Academy, and the Optical Society of America. He received the 1996 Presidential Early Career Award for Scientists and Engineers from the White House, the 1996 Early Career Research Award from the Environmental Protection Agency, the 1997 CAREER Award from the National Science Foundation, and the 2017 ACES Technical Achievement Award. He also served as a Guest Editor for the PROCEEDINGS OF THE IEEE. Since 2015, he has been the Founding Editor-in-Chief of the new IEEE JOURNAL ON MULTISCALE AND MULTIPHYSICS COMPUTATIONAL TECHNIQUES. He served as an IEEE Antennas and Propagation Society Distinguished Lecturer from 2014 to 2016. Currently, he serves as the Deputy Editor-in-Chief for the *Progress in Electromagnetics Research*, an Associate Editor for the IEEE TRANSACTIONS ON GEOSCIENCE AND REMOTE SENSING, and an Editor for the *Journal of Computational Acoustics*.